

Progress Toward use of a Dense Plasma Focus as a Light Source for Production EUV Lithography

W.N. Partlo, I.V. Fomenkov, R.M. Ness, R.I. Oliver, S.T. Melnychuk, J.E. Rauch

Cymer Inc., 16750 Via Del Campo Crt., San Diego, CA 92127

ABSTRACT

Recent advances in the Dense Plasma Focus (DPF) under investigation by Cymer as an EUV light source have increased both the total energy storage capacity and the peak drive current. Previous generation DPF tools built by Cymer produced no measurable EUV radiation while employing Xenon as a source gas, but instead employed Lithium vapor due to its higher emission efficiency at low plasma temperatures. With Xenon as a source gas, this generation DPF exhibits efficiency similar to other sources employing direct electrical drive of the Xenon plasma. An emission efficiency of greater than 0.20% has been measured into 2π str and a 2% bandwidth centered at 13.5nm.

Other characteristics of this DPF have been measured such as energy stability, spectrum, source size, position stability, and operation at high repetition rates. In addition, the out-of-band radiation in the UV/Vis region (130nm-1300nm) has been measured and found to be only 0.38% of all radiation emitted by this source. Such low out-of-band radiation opens up the possibility of eliminating the Spectral Purity Filter and the problems associated with its use.

This source concept does not use a multi-layer dielectric mirror as the first collector, but instead employs a grazing incidence collector that is more tolerant to debris. Progress has been made in the fabrication quality of this optic. Recent measurements of prototypes show that this optic will not degrade the source brightness. Also, a more efficient design has been created that consist of two shells coated with Ruthenium. This design collects and re-images 18.6% of the EUV radiation emitted into 2π str.

Keywords: EUV Lithography, Dense Plasma Focus, Solid State Pulse Power, Xenon Emission

1. INTRODUCTION

Researchers at Cymer have pursued development of a DPF as an EUV light source for microlithography because it falls in the middle ground of stored energy for EUV sources. Machines with large stored energies ($\geq 100\text{J}$) will be difficult to scale to the multi-kHz repetitions rates required for scanner-based lithography tools and machines with small input energies ($\leq 1\text{J}$) will require very high repetition rates. Also as a practical matter, the proven and production-worthy solid state pulse power technology used in Cymer's excimer lasers is well suited for the 10-20J stored energy requirements of this DPF.

Initial research efforts focused on a DPF that produced plasma temperatures appropriate for the 13.5nm emission line of doubly ionized Lithium¹. In order to de-couple the development of Lithium handling and delivery from the development of basic DPF performance, a 4th generation machine was created that produces significantly higher plasma temperatures. With this machine, efficient EUV emission with Xenon has been achieved and DPF development can now proceed in parallel with the development of Lithium as a source element.

This 4th generation machine is flexible enough to allow quick changes to the electrode geometry, source gas, buffer gas, gas feed mechanisms, and drive energy. All of these factors have been found to be important for efficient and stable DPF operation.

Operation with Xenon as the source gas, instead of Lithium, still requires the use of a first collector tolerant to debris. It is unreasonable to expect the electrode erosion to be zero. Thus, success of this source concept depends on fabrication of the grazing incidence optic proposed as a collector element more tolerant to debris than a multi-layer dielectric mirror. First

prototypes of this optic exhibited poor imaging quality such that they degraded the source brightness. Recent prototypes are significantly better to the point where they will have little impact on the source brightness.

2. DENSE PLASMA FOCUS SYSTEM DESCRIPTION

Previous generations of DPFs developed by Cymer employed no electrical pulse compression. That is, the capacitor with the DC stored energy was tied directly to the final capacitor stage. In such an arrangement, the power flow onto the last stage capacitor is limited by the peak current capability of the solid state switch placed between these two stages. By inserting a magnetic compression stage (LS2 in Fig 1), similar to that used in Cymer's excimer lasers, the peak power flow into the final stage capacitor can be greatly increased since it is no longer limited by the current capability of the solid state switch.

Another limitation of previous generation machines was the voltage level applied to the last stage capacitors. With no step up transformer, this voltage was limited to the rating of the solid state switch. For the 4th generation machine, an inductive voltage adder was inserted between the C1 and C2 stages to allow higher voltage operation on C2 without limitations from the solid state switch.

With the configuration shown in Fig 1, the transfer time of energy onto C2 is approximately 500ns. The step-up ratio for the transformer is set to 4X which allows a maximum voltage on C2 of 4.5kV, compared to 1.3kV on previous generation machines. Running at the maximum C2 voltage, this machine can deliver 13.5J of energy to the DPF electrodes.

The LS3 saturable reactor between C2 and the DPF electrodes performs two functions. The first is to hold off current flow between C2 and the electrodes until full energy transfer onto C2 has occurred. The second function is to act as a diode for reverse current, preventing current flow during the voltage overshoot phase. Fig 2 shows the measured waveshapes for typical operation. C2 is charged to approximately 4.5kV while the LS3 reactor holds off current flow into the anode. Once LS3 saturates, the full C2 voltage is quickly applied to the anode with a rise time of approximately 50ns. Current flowing through the plasma drains C2 and because of imperfect impedance matching the voltage on C2 overshoots. Once the voltage overshoots, LS3 prevents reverse current and thus the voltage on the anode drops to zero. The overshoot energy stored on C2 travels back through the solid state compression circuit, is recovered on C0, and is available for use in the next pulse.

The pinch event that produces EUV radiation occurs near the zero crossing of the C2 voltage waveshape as shown in Fig 2. The current is a maximum at this point in the waveshape and thus the highest plasma temperature is reached under these conditions. The timing of the pinch event to the C2 waveshape depends on many factors; the voltage on C2, the size of C2, the inductance between C2 and the electrodes, the rundown length of the anode, the inner and outer diameter of the anode, and the gas density between the anode and the cathode. At this time we are still investigating the scaling rules that apply to each of these factors.

Optimization of the whole source must consider more than just the peak current produced during the pinch. For example, the anode geometry is driven by more than just electrical factors. The thermal engineering for high duty cycle operation favors a short anode with a large diameter. As a second example, the gas recipe must be optimized for best pinch performance but also with consideration of absorption of the EUV radiation produced by the pinch.

3. EMISSION SPECTRA OF VARIOUS SOURCE GASES

The design of this DPF allows us to separate the functions of the source gas from that of the buffer gas. As shown in Fig 3, a feed tube running down the center of the hollow anode provides the source gas while the buffer gas is supplied to the main vessel. The buffer gas flow is adjusted via pressure feed-back from a sensor attached to the main vessel. The source gas flow is controlled with a mass flow controller. For a given source gas and buffer gas, the vessel pressure and source gas flow rate are adjusted for the best compromise between stability and EUV output.

The flexibility of this design allowed us to quickly investigate several source gases. The source gases investigated were Argon, Neon, Krypton, Oxygen, and Xenon. Oxygen and Xenon have been proposed as potential EUV source gases because they possess emission lines within the reflectivity band of EUV multi-layer dielectric mirrors. The measured spectra for Argon, Neon, and Krypton are shown in Figs 4 through 6. Some of the emission lines are identified along with the energy

required to get to this ionization level from the previous ionization level. Though none of these gases show promise as an EUV source gas, these results show that this DPF can create ionized species requiring several hundred eV of energy.

The measured spectrum for Oxygen is shown in Fig 7. The 2p-4d transition of Oxygen VI is highlighted on the graph. This transition has been proposed as an EUV source since it is narrow band and falls within the multi-layer mirror bandwidth². Unfortunately, the emission of this line as excited by the DPF is very weak. The spectrometer signal level for this emission line is 100 times lower than some of the lines for Argon, Neon, Krypton. This is an unexpected result since other researchers have found this line to be relatively intense. We suspect that part of the problem is related to the fact that this is a diatomic gas. When running with Oxygen and Nitrogen, the only two diatomic gases tried so far, the pinch stability was very poor and the EUV output was low for both. At this time, there is limited understanding of this effect.

The measured Xenon spectrum is shown in Fig 8 along with the published reflectivity of an EUV Mo/Si multi-layer dielectric mirror³. The resolution of this scanning slit spectrometer is sufficient to resolve many of the lines that make up the cluster of Xenon XI emission near 13.5nm. It is interesting to note that the Xenon spectrum sits on an unresolved baseline. Only Krypton showed a similar result and then only for a limited spectral region between 8.5nm and 11nm.

We took Xenon spectral scans with two different input energies in order to observe the relative impact to each of the emission clusters, shown in Fig 9⁴. Changing the input energy by 35% from 7.7J to 10.4J increased the emission from the Xenon IX lines by only 30%, but the emission from the Xenon XI lines increased by 220%. This result leads us to believe that we do not exceed the efficient plasma temperature for 13.5nm emission with Xenon even with the highest input energy available from this DPF.

4. ABSOLUTE IN-BAND EUV EMISSION MEASUREMENTS

A measurement vessel based on the concept used by FOM for the ASML "flying circus" was constructed to make measurements of the in-band EUV emission with Xenon source gas⁵. The experimental setup is shown in Fig 10. A second vacuum vessel is attached to the main vessel with a small diameter tube connecting the two. The end of this tube is placed 5 cm from the pinch and the measurement vessel is differentially pumped with a turbo-molecular pump.

Radiation traveling along the axis passes through two apertures and is reflected from a Mo/Si multi-layer mirror located 92 cm from the source. The reflection from this mirror is directed through a Beryllium foil and onto an uncoated IRD AXUV-100 photodiode. The Beryllium foil blocks any visible radiation that might be reflected from the Mo/Si mirror. The mirror is curved so that it focuses radiation to a small spot on the diode. Thus, the 5 mm diameter aperture directly in front of the mirror controls the acceptance angle of this measurement setup. The spherical expansion factor relative to 2π str for this arrangement is thus;

$$SE_{\text{factor}} = \frac{\pi(.5/2)^2}{2\pi(92)^2} = 3.69 \cdot 10^{-6}.$$

Gas absorption in the measurement vessel is kept to a minimum by the differential pumping that maintains the pressure in this region to 6 mTorr or less. We assume no gas absorption in the measurement vessel. In the energy calculations, we do not compensate for the absorption due to the 5 cm length of gas between the pinch and the connecting tube since this absorption is unavoidable in a production machine. For a production machine, it is proposed that a foil trap be placed 5 cm from the source⁶. This foil trap will serve two purposes, the first is to stop debris generated by the DPF from reaching the collector. The second function of the foil trap is to allow differential pumping between the pinch region and the collector region. The connecting tube between the main vessel and the measurement vessel simulates the pressure drop expected across the foil trap.

The peak reflectivity of the Mo/Si mirror is assumed to be 67% with a central wavelength of 13.5nm. This assumption is the most conservative possible since this value is the theoretical reflectivity. In addition, this mirror is assumed to have a 4% bandwidth. All calculations include a reduction factor of 2 to account for the effective 2% bandwidth due to the serial reflectivity of the 9 Mo/Si mirrors in a production EUV lithography tool.

The Beryllium foil was purchased with a nominal thickness of 1.0 μm . The calculated transmission of a 1.0 μm thick Beryllium foil at 13.5nm is 17.4%. To ensure a more accurate energy measurement, we measured the transmission of this

foil by making Xenon spectral scans with and without this foil placed at the inlet to the spectrometer. The results of these scans are shown in Fig 11. Taking the ratio of these two scans and fitting to the published transmission of Beryllium results in an effective thickness for this foil of 0.8 μm and a transmission at 13.5nm of 25.1%. Discussions with the vendor for this foil highlighted the fact that there is tolerance on the actual thickness and that the Beryllium can oxidize and thus change its effective thickness. All energy measurements stated in this paper assume a foil transmission of 25.1%.

Finally, the IRD photodiode quantum efficiency is assumed to be that published for this type of diode, 21.4 electrons/photon at 13.5nm.

Using this setup, we measured the emission into 2π str, 2% bandwidth versus input energy with Xenon as a source gas. The resulting energy output and efficiency curves are shown in Fig 12. The most notable result obtained from this data is that the efficiency continues to rise even at the maximum input energy. Unfortunately, the components in this DPF limit the maximum input energy at 10.5J, thus the highest efficiency to date for this machine is 0.23%. The efficiency curve does show some evidence of rolling over, so it is unclear how much more improvement is available at higher input energies.

5. ENERGY STABILITY MEASUREMENTS

An important performance parameter for any EUV lithography source is emission stability. All EUV lithography tools will be scanner based and the slit width of an all-reflective projection optic is expected to be more narrow than that for a conventional all-refractive projection optic. A narrow scanning slit allows only a limited number of pulses per sub-exposure region. The current published requirement for energy stability is $3\sigma < 2\%$.

Using the setup described in the previous section, the emission stability of the DPF was measured at low repetition rate and high repetition rate. The low repetition rate data is shown in Fig 13 with a resulting $1\sigma = 18.3\%$, very far from the stated requirements. To better understand the sources of instability, the emission was measured at 1000Hz and compared to the 20Hz data. The measured data for 100 pulse bursts at 1000Hz is shown in Fig 14. The measured standard deviation for energy variation at 1000Hz is 16.2%. A comparison between the 20Hz behavior and the 1000Hz behavior gives potential insight to the cause(s) of instability. Many proposed mechanisms for instability are repetition rate dependent and thus the 1000Hz performance would be degraded compared to the 20Hz data. Such is not the case and thus mechanisms that are repetition rate independent seem to dominate.

The 1000Hz burst data of Fig 14 also shows the burst transient behavior found on previous generation machines. We have not yet demonstrated conclusively the cause of this burst transient.

6. OUT-OF-BAND EMISSION MEASUREMENTS

Another important consideration for a production EUV source is the out-of-band emission. Since the Mo/Si mirrors also exhibit reasonable reflectivity in the UV/Vis region, energy in this wavelength range can make it to the wafer plane and degrade the aerial image. To eliminate radiation from this spectral region, a Spectral Purity Filter (SPF) has been proposed. This filter, consisting of a thin membrane of Silicon or Zirconium, would have an extinction coefficient of many orders for UV/Vis but only 50% for 13.5nm radiation.

To measure the out-of-band radiation, a setup as shown in Fig 15 was constructed. An uncoated IRD photodiode was used as the detector. The only practical method for attenuating all wavelengths from the source equally is to use propagation through vacuum. Since the source is assumed isotropic in its emission (see next section for details), simple spherical expansion can be used to reduce the intensity on the uncoated photodiode down to reasonable levels.

By placing different filters in the beam path we can select different spectral regions for evaluation. The two filters used in these measurements were a Beryllium foil and a CaF₂ plate. The Beryllium foil transmits over a range between 11nm and 20nm. The CaF₂ plate transmits over a range between 130nm and 1300nm. The results for these measurements are as follows:

| | |
|--------------------------------|-------------------------------|
| Emission into all wavelengths: | 211 mJ (2.0% of input energy) |
|--------------------------------|-------------------------------|

| | |
|----------------------------------|---------------------------------|
| Emission into 11nm-20nm band: | 110 mJ (1.0% of input energy) |
| Emission into 130nm-1300nm band: | 0.8 mJ (0.38% of all radiation) |

There are two surprising results in this data set. The first is that so little of the input energy is converted to radiation from the pinch. There are other sources of radiation, such as the plasma between the anode and cathode, but this radiation will not be re-imaged by the collector and thus will not make it into the exposure tool. With such a small percentage of the input energy emitted as radiation from the pinch, there is potential for significant in-band efficiency improvements once the mechanisms for the other 98% energy consumption are identified. Examples of known loss mechanisms are capacitor internal resistance, anode fall, cathode fall, and ion velocity (i.e. thrust)⁷⁻⁹.

The second surprising result is the very small fraction of radiation emitted in the UV/Vis region. This result was at first suspicious until it was realized that there are certain operating conditions (gas recipe and input energy) that produce significant amounts of in-band EUV radiation but no observable visible emission. Observations through a window in the vessel confirm that under certain conditions there is no visible pinch at all!

Such low UV/Vis radiation allows the possibility of eliminating the SPF. There are two advantages to be gained by eliminating this component. The first advantage is avoiding the 50% insertion loss caused by this filter for the in-band EUV radiation. Exposure tools designed with a SPF that require 40-60W of in-band radiation would then only require 20-30W. The second advantage to eliminating this component is the challenging thermal issues associated with use of this foil. The absorbed power into this very thin foil while passing 40-60W of in-band EUV radiation can raise the temperature of the foil beyond its melting point.

7. EUV SOURCE IMAGES

Due to the relatively low NA of the projection optics proposed for EUV lithography tools, the source must exhibit high brightness. If the size of the source is too large then the allowed collection angle will be limited.

A pinhole camera arrangement shown in Fig 16 was used to make EUV images of the DPF with Xenon as the source gas. This pinhole camera arrangement has an adjustable viewing angle between on-axis and 30° off axis. The resulting source images for several angles are shown in Fig 17. These images are an integration of 1000 pulses so as to average out any source position instabilities. As the camera is moved further off axis, the source image becomes elongated to the point where at 30° the source is 250 μm X 1700 μm FWHM.

By integrating the total charge accumulated by the CCD array at each angle we can get an idea of the isotropic nature of the source. Fig 18 shows cross-section slices of the EUV image for each angle as well as a polar plot of the measured charge on the CCD array. To within $\pm 7.5\%$ the source can be considered isotropic.

8. GRAZING INCIDENCE COLLECTOR

As important as creating an EUV source with high spectral brightness is collecting and relaying this radiation to a region safe for use with the sensitive Mo/Si EUV mirrors. Since this DPF source is expected to suffer from electrode erosion, Mo/Si multi-layer EUV mirrors will degrade under direct exposure to this debris, so an alternate collection optic is required. Use of a collector based on grazing incidence reflections offers promise because such an optic exhibits high reflectivity and can be fabricated from materials that are less sensitive to deposition of debris. In addition, if the design of the grazing incidence collector is made simple enough, it can be a low cost replacement part.

The original concept for this optic was to have it collect source radiation and form a collimated beam. Such an optic would have a parabolic shape. More recent concepts of an optimized source configuration employ an optic that collects the source radiation and re-images it through a small hole in the vessel that separates the source from the illumination optics. The shape of this optic is elliptical.

The visible imaging performance of the first prototype elliptical grazing incidence optic is shown in Fig 19. The image of the left is the result at best focus and the image on the right is 9 mm from best focus. The image at best focus is a near perfect

replica of the 50 μm source spot used to illuminate the optic. The dark center in the out of focus image is due to the fact that this is only a single shell optic and the rays near the axis are not captured and reflected toward the image point. A multi-shell optic would fill in this dark region. The undulations seen in the out of focus image are caused by imperfections in the elliptical surface.

A ray-trace program has been developed that assists in optimizing the design and performance of these optics. The reflectivity loss versus angle for a chosen coating material is modeled as well as the ray deviations caused by imperfections from the desired perfect surface. Fig 20 shows the measured intensity for one side of the out of focus image along with a simulated intensity pattern. The simulated pattern was produced by perturbing the elliptical surface with rotationally symmetric gaussian shapes between 0.5 μm and 2.2 μm in magnitude. The location, height, and width of these perturbations are shown in the table accompanying Fig 20. These simulated values are in agreement with the vendor's own measurements of the surface imperfections.

This ray-trace program has also been used to develop a more efficient collector design. The original concept was to use a Molybdenum coating because it exhibits the highest grazing incidence reflectivity for angles below 20° . By allowing the focal length and optic length to be free parameters and investigating the use of other coating materials such as Ruthenium, an optic design with greater geometric collection efficiency and greater overall efficiency was been developed. The following are details for this design:

| | |
|--|---|
| Collector Output | Imaging (Elliptical Shells) |
| Number of Shells | 2 |
| Source to Image Distance | 400 mm |
| Focal Length | 200mm |
| Distance to optic entrance | 50mm |
| Number of reflections | 1 |
| Mirror coating material | Ruthenium |
| Grazing angle | (outer shell): 19.6° - 26.8° (inner shell): 7.4° - 11.0° |
| Collector length | 150mm |
| Geometrical collection | 28.6% of 2π (two shells) |
| Overall collection efficiency (including reflection losses) | 18.6% of 2π (two shells) |

9. CONCLUSIONS

The following calculations combine the parameters discussed above to give the maximum in-band, collectable source power with this generation DPF and Xenon as a source gas:

| | |
|---|-------|
| Thermally limited input power: | 25kW |
| Conversion efficiency into 2.0% BW in-band, 2π str: | 0.20% |
| Overall collection efficiency (of 2π): | 18.6% |
| Maximum collectable, in-band, 13.5nm power: | 9.3W |

This last year's work has produced the following important observations.

Positive Aspects

- The 4th generation DPF exhibits conversion efficiencies with Xenon comparable to other direct electrical excitation sources.
- The quality of the grazing incidence collection optics has improved such that it no longer degrades the source brightness.
- The out-of-band UV/Vis radiation produced by this DPF is very low and likely means the elimination of the SPF.

Negative Aspects

- The current output energy stability is poor and needs improvement.
- Due to present thermal limits, the maximum expected in-band, collectable, 13.5nm optical power is approximately 9W with Xenon as a source gas.
- Initial experiments show electrode erosion to be a factor requiring a debris mitigation scheme.

10. ACKNOWLEDGMENTS

The authors would like to acknowledge the immeasurable contributions made by Daniel Birx who died with his wife, Karen, in the crash of their home-built aircraft.

Many of us in the scientific, engineering, and manufacturing areas came to know and deeply respect Dan. His expertise in the field of high voltage pulsed power was unequalled. His enthusiasm for solving problems was infectious and his example has made an immeasurable impact on many of us at Cymer. He lived his life with the same drive that he gave his work. Rare is the man with so much intelligence, diligence, capacity for joy, and respect for life. The world has lost a brilliant individual, and many of us lost a very close and dear friend. It is an honor and a privilege to have known him.

To honor his memory, the newly built and commissioned research facility on the Cymer campus in San Diego has been named "The Birx Research Center".

11. REFERENCES

1. W. Partlo, et. al., "Development of an EUV (13.5nm) Light Source Employing a Dense Plasma Focus in Lithium Vapor," *Proc. of SPIE*, vol. 3997, Feb. 2000.
2. F. Jin and M. Richardson, "Conversion Efficiency and debris studies of ice targets for EUV projection lithography," *OSA Proceedings on Extreme Lithography*, vol. 23, No. 260, 1995.
3. Lawrence Berkeley Labs web sight: http://www-cxro.lbl.gov/optical_constants/
4. M. McGeoch, "Radio-frequency-preionized Xenon Z-pinch Source for Extreme Ultraviolet Lithography," *Applied Optics*, Vol. 37, No.9, March 1998.
5. R. Stuik, et. al., "Flying Circus EUV Source Comparison," *Presented at the EUV source workshop sponsored by Sematech*, Nov. 2000.
6. L. Shmaenok, et. al., "Demonstration of a Foil Trap Technique to Eliminate Laser Plasma Debris and Small Particles," *Proc. of SPIE*, vol. 3331, Feb. 1998.
7. J. Ziemer, E. Cubbin, E. Choueiri, and D. Birx, "Performance Characterization of a High Efficiency Gas-Fed Pulsed Plasma Thruster," *33rd AIAA/ASME/SAE/ASEE Joint Propulsion Conference*, Seattle, WA, 1997.
8. J. Ziemer, E. Choueiri, and D. Birx, "Trends in Performance Improvements of a Gas-Fed Pulsed Plasma Thruster," *25th International Electric Propulsion Conference*, Cleveland, OH, 1997.
9. D. Birx, "Plasma Gun and Methods for the use Thereof," *US Patent 5,866,871*, Feb. 2, 1999.

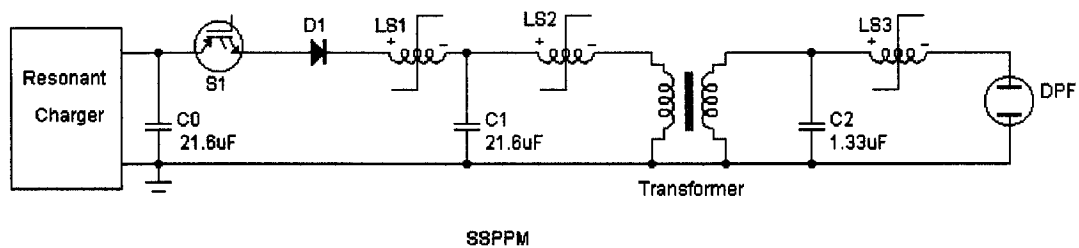


Fig 1. Generation 4 Dense Plasma Focus Schematic.

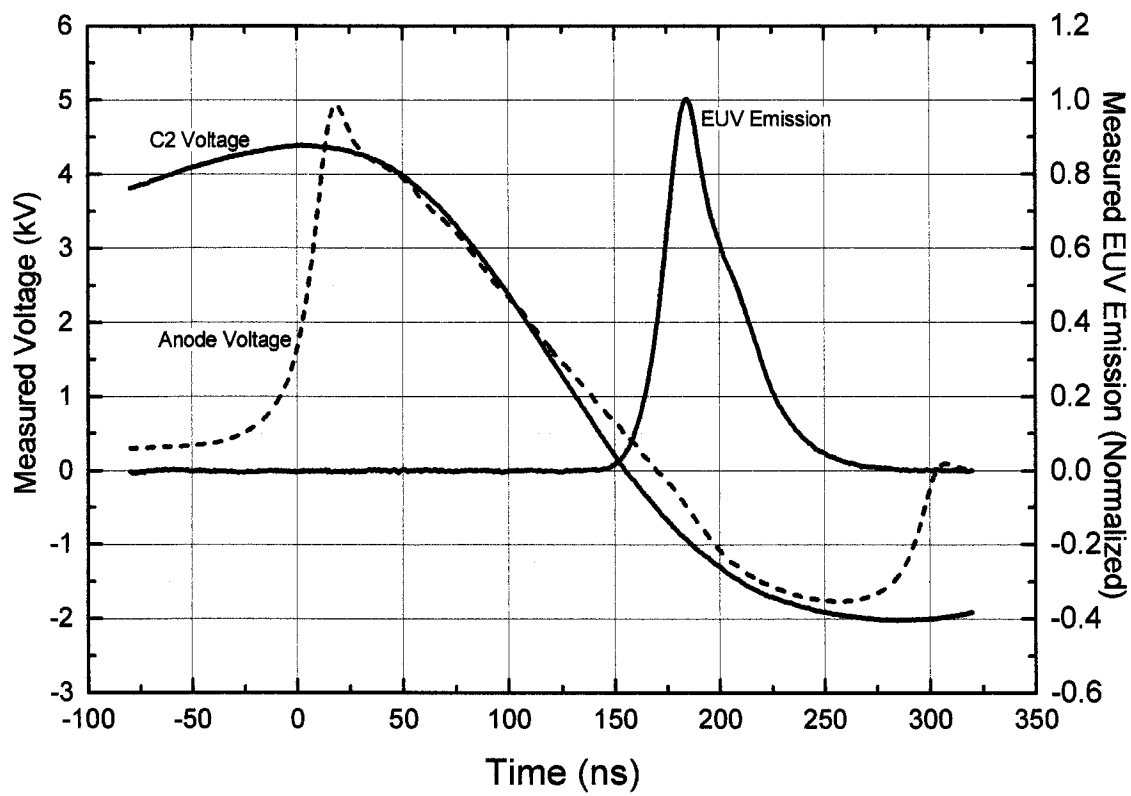


Fig 2. Voltage and emission waveshapes for generation 4 DPF.

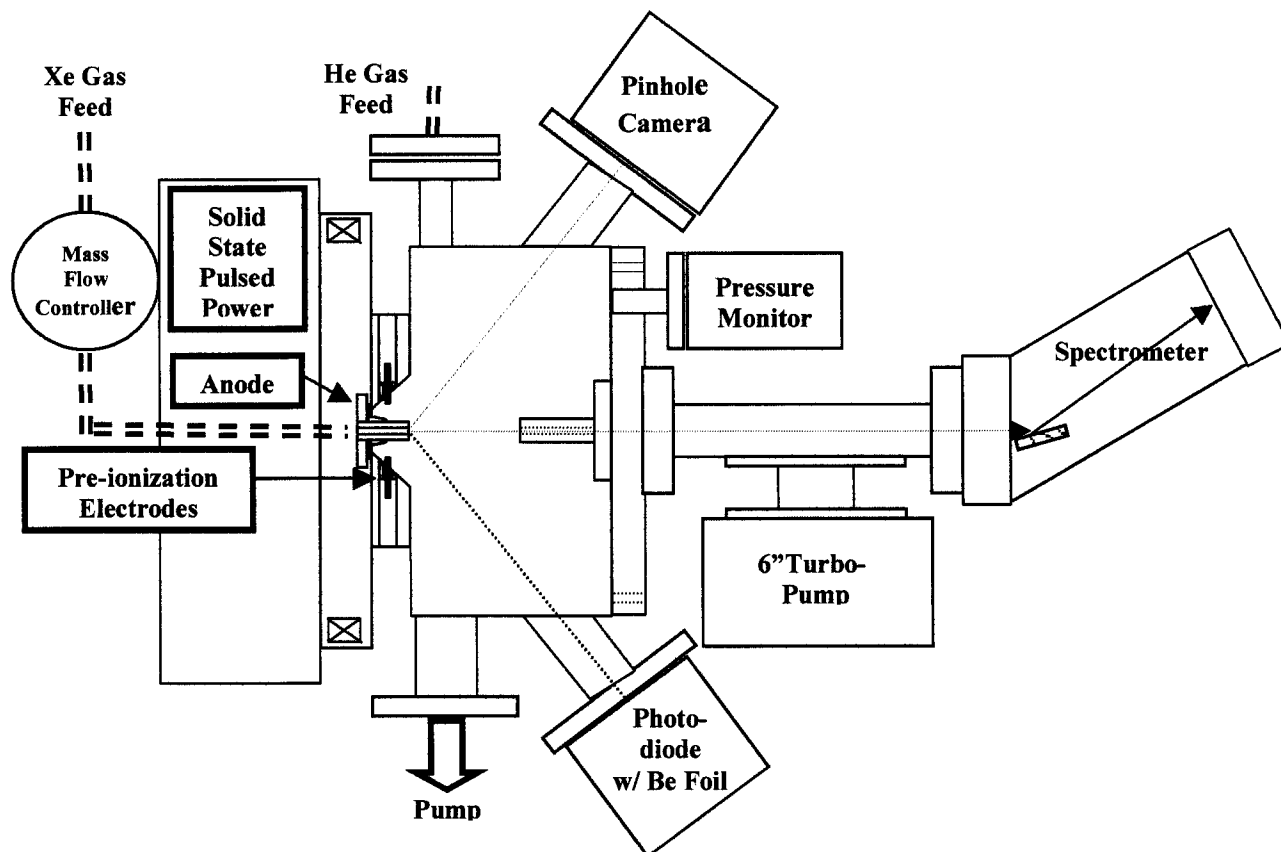


Fig 3. Experimental setup showing attached grazing incidence scanning spectrometer.

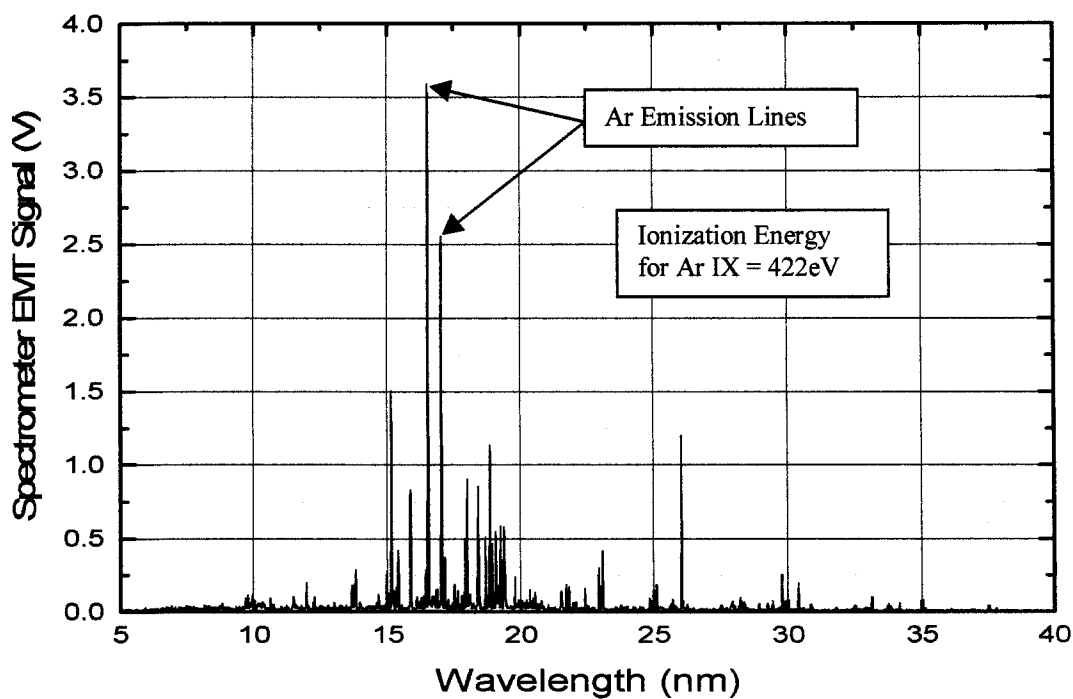


Fig 4. Measured EUV spectrum of Argon.

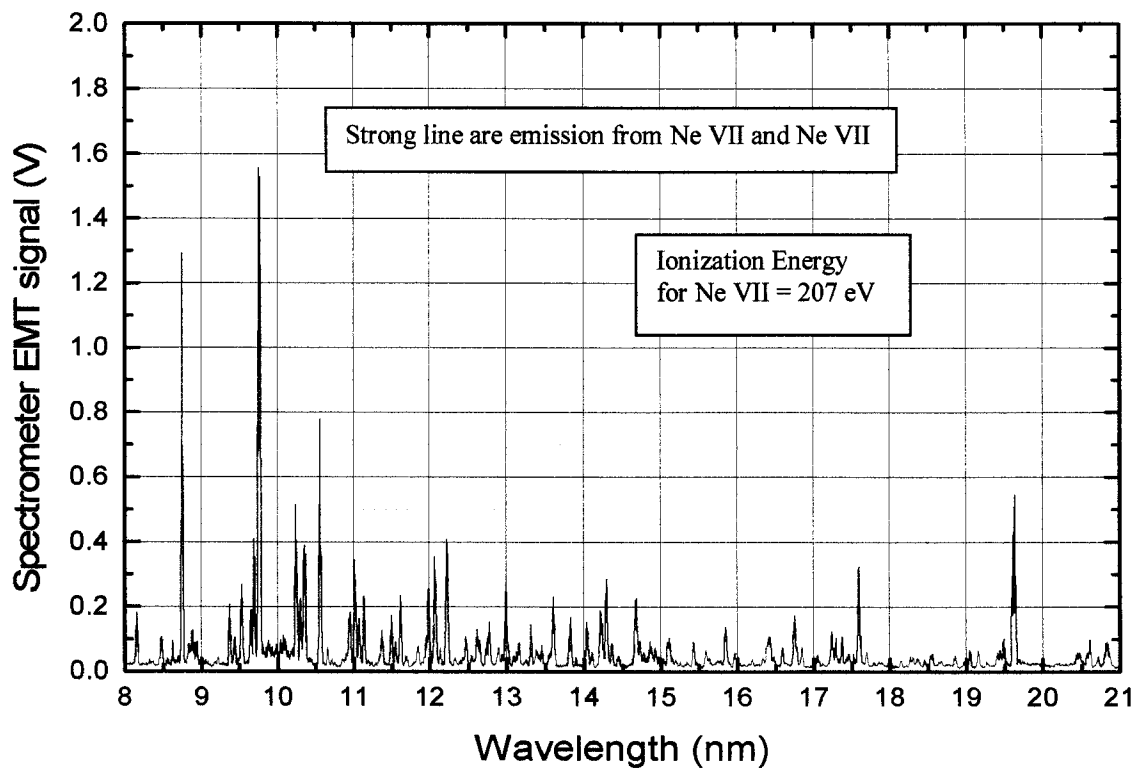


Fig 5. Measured EUV spectrum of Neon.

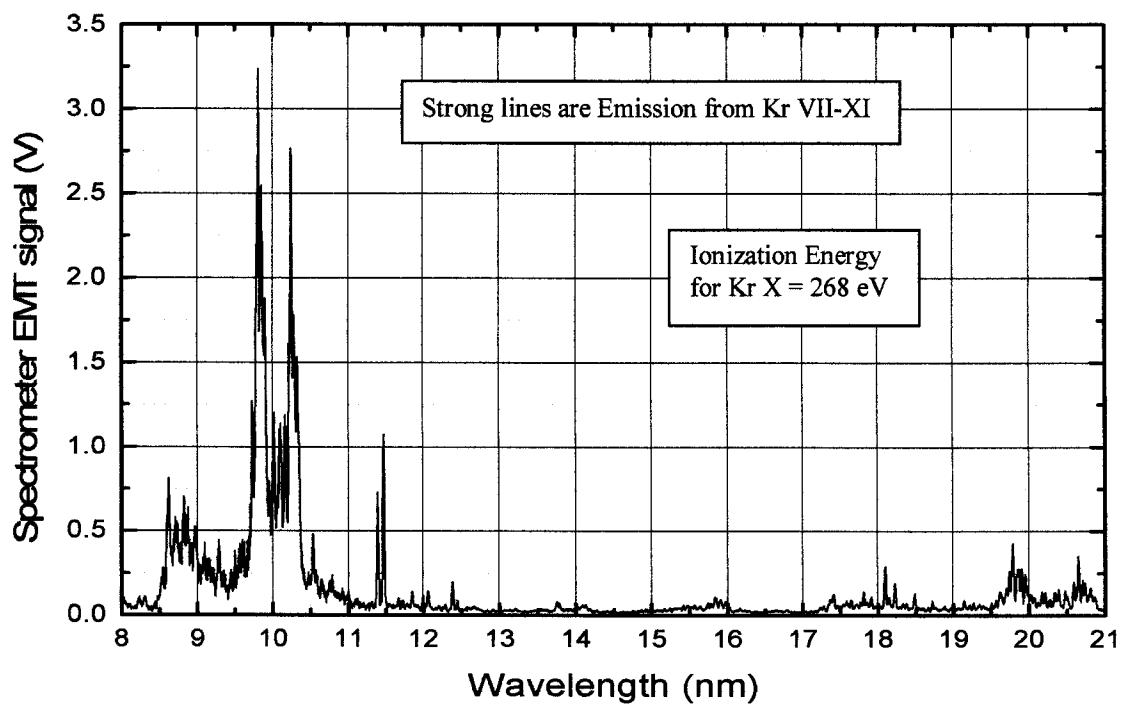


Fig 6. Measured EUV spectrum of Krypton.

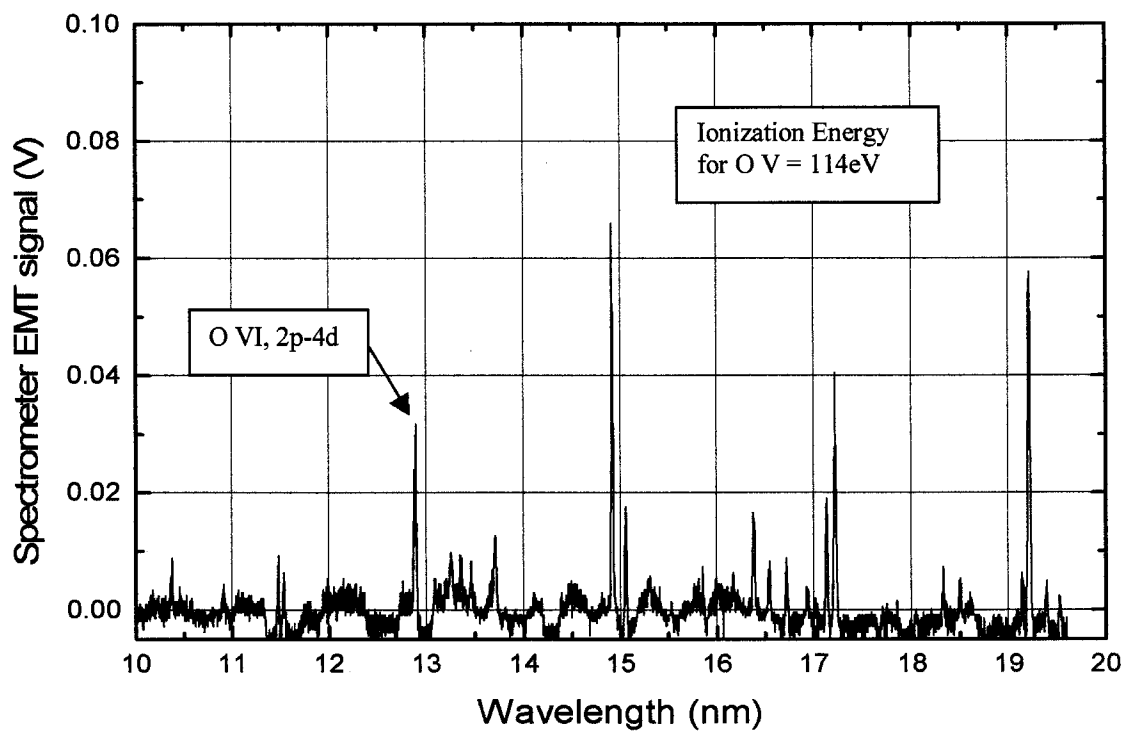


Fig 7. Measured EUV spectrum of Oxygen.

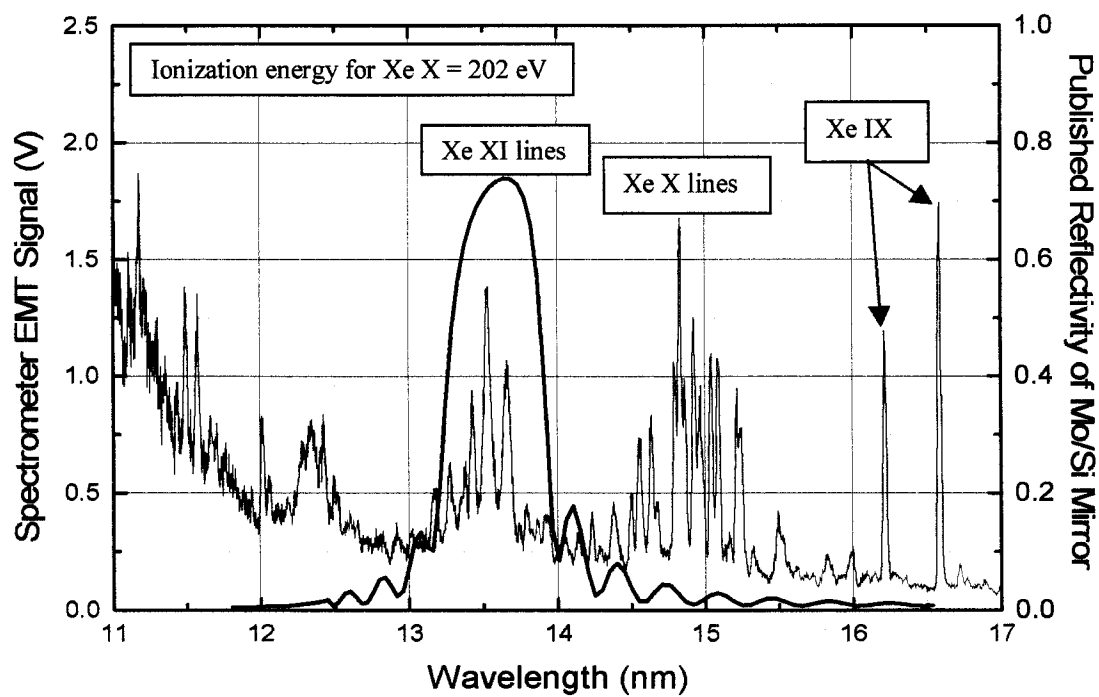


Fig 8. Measured EUV spectrum for Xenon.

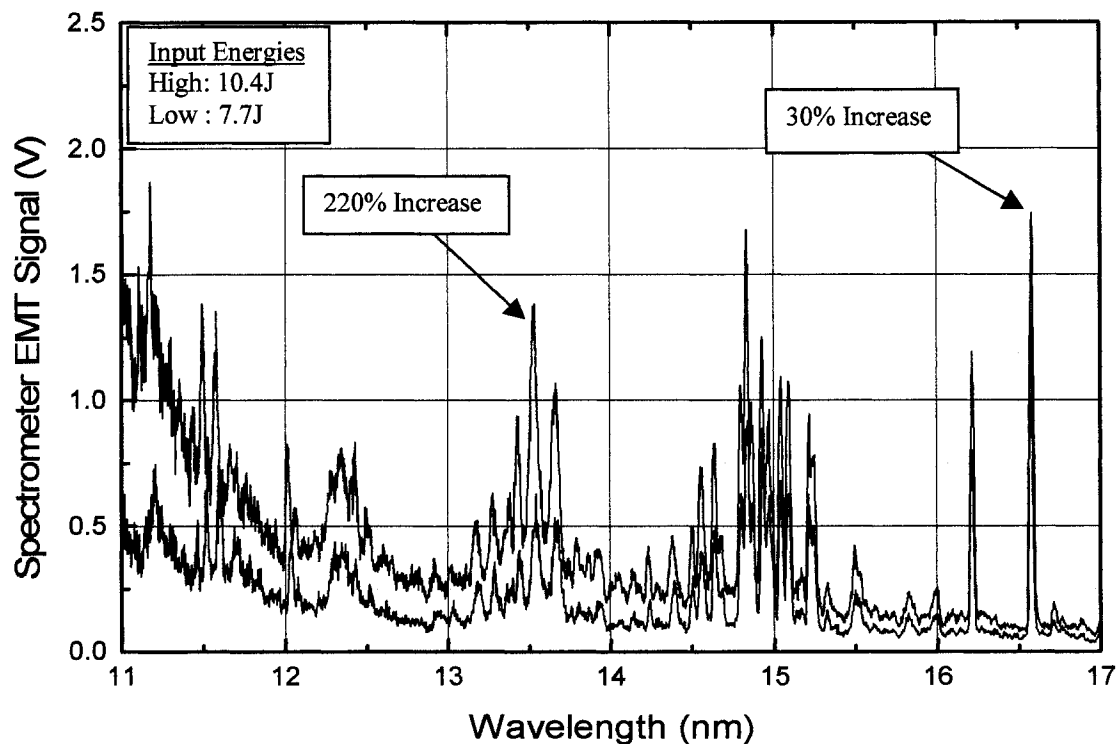


Fig 9. Measured EUV spectrum of Xenon for two different input energies.

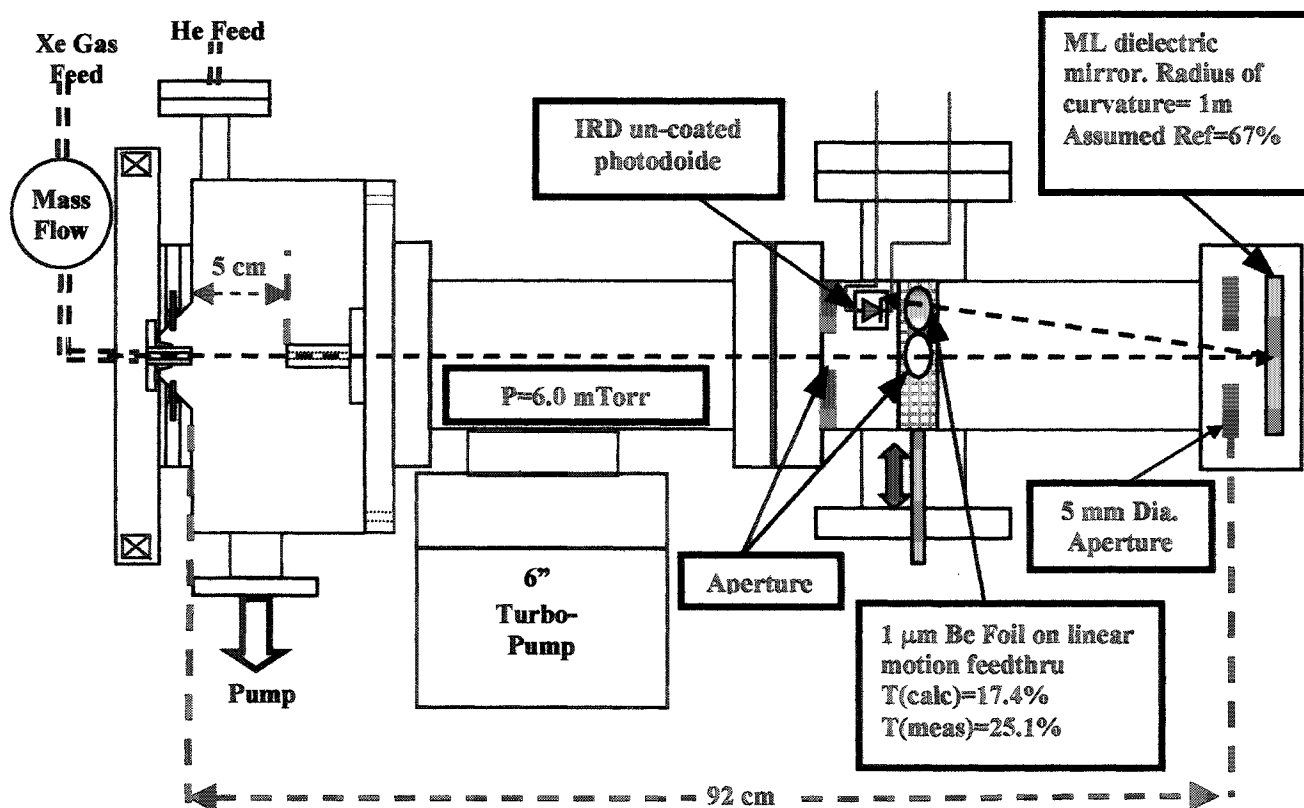


Fig 10. Experimental setup used to measure in-band 13.5nm emission.

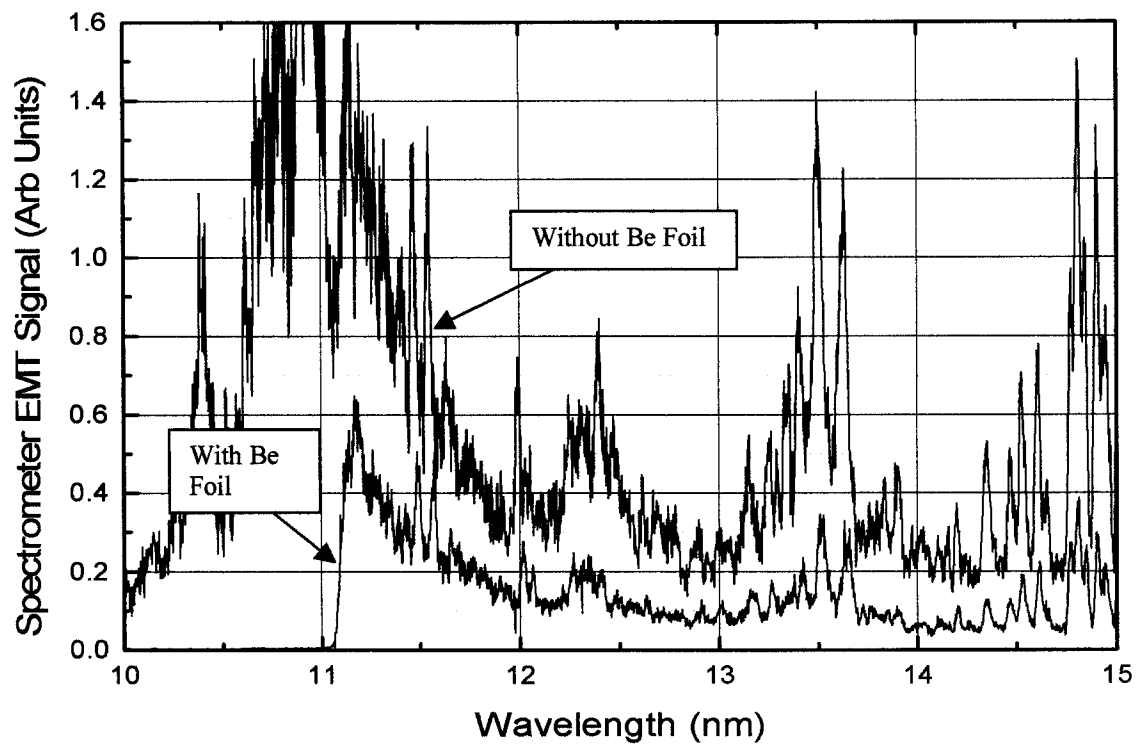


Fig 11. EUV Spectral scans of Xenon with and without a Beryllium foil in line.

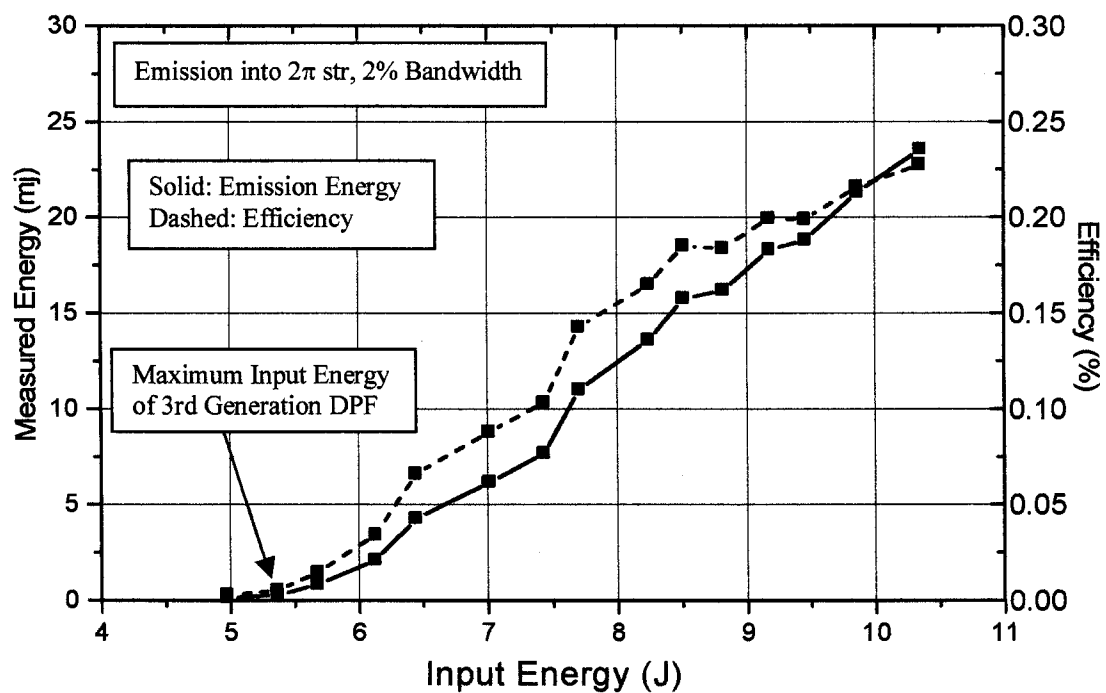


Fig 12. Measured in-band 13.5nm emission vs. input energy with Xenon source gas.

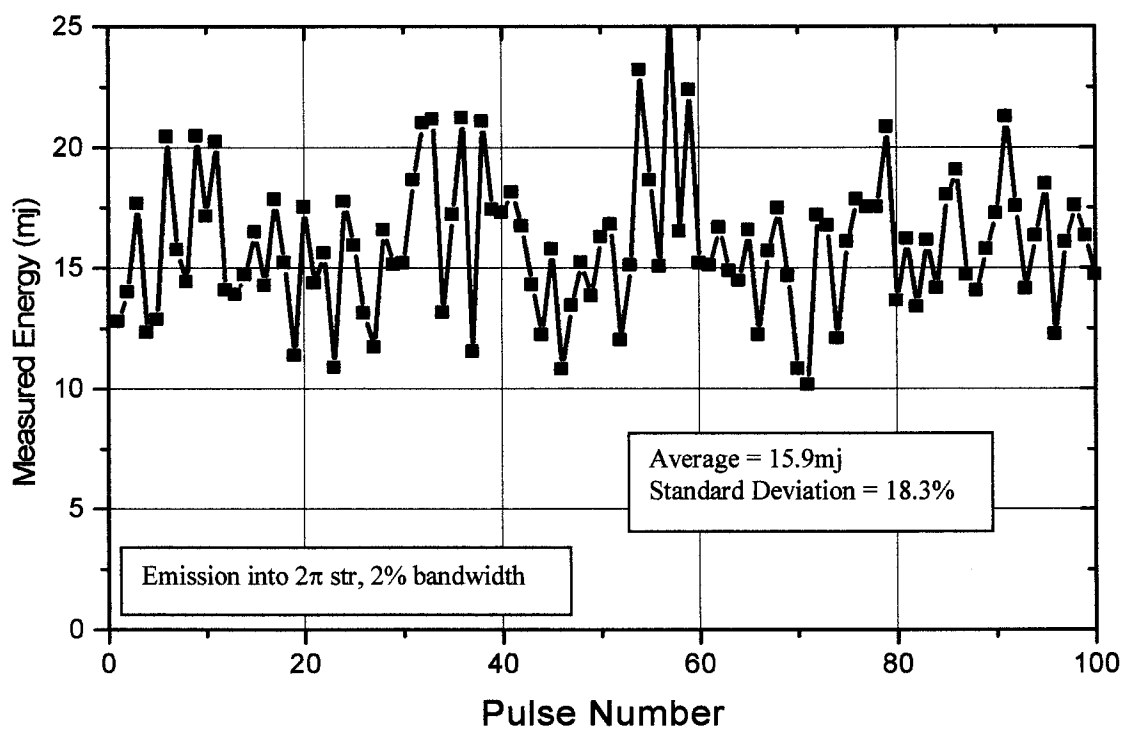


Fig 13. Measured in-band emission stability at 20Hz with Xenon source gas.

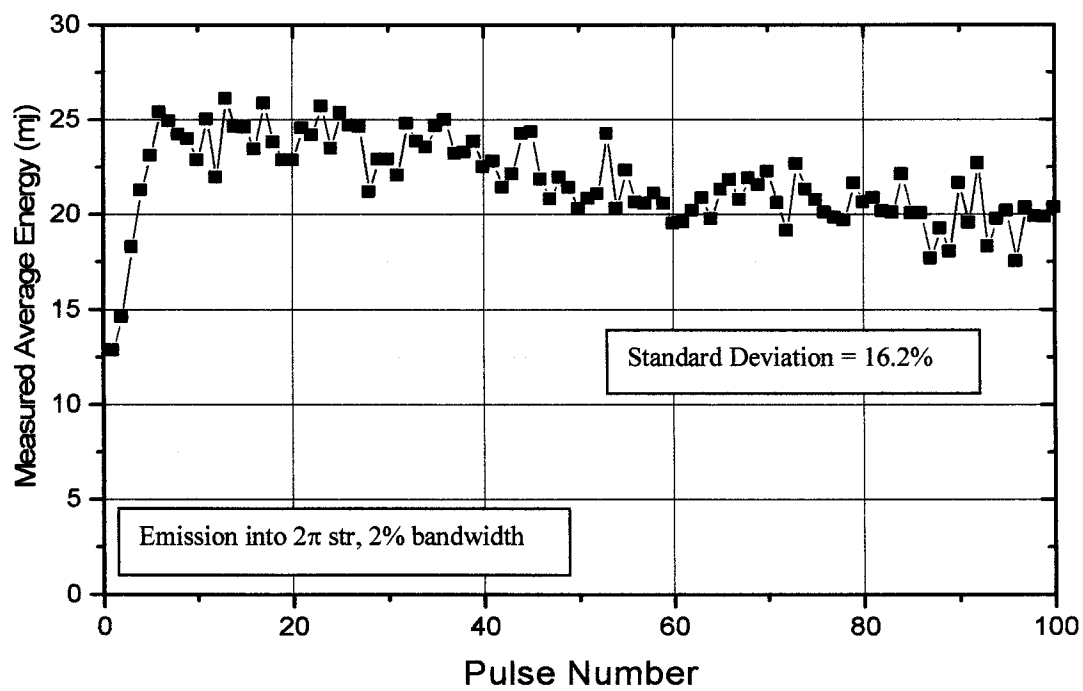


Fig 14. Measured in-band emission at 1000Hz with Xenon source gas.

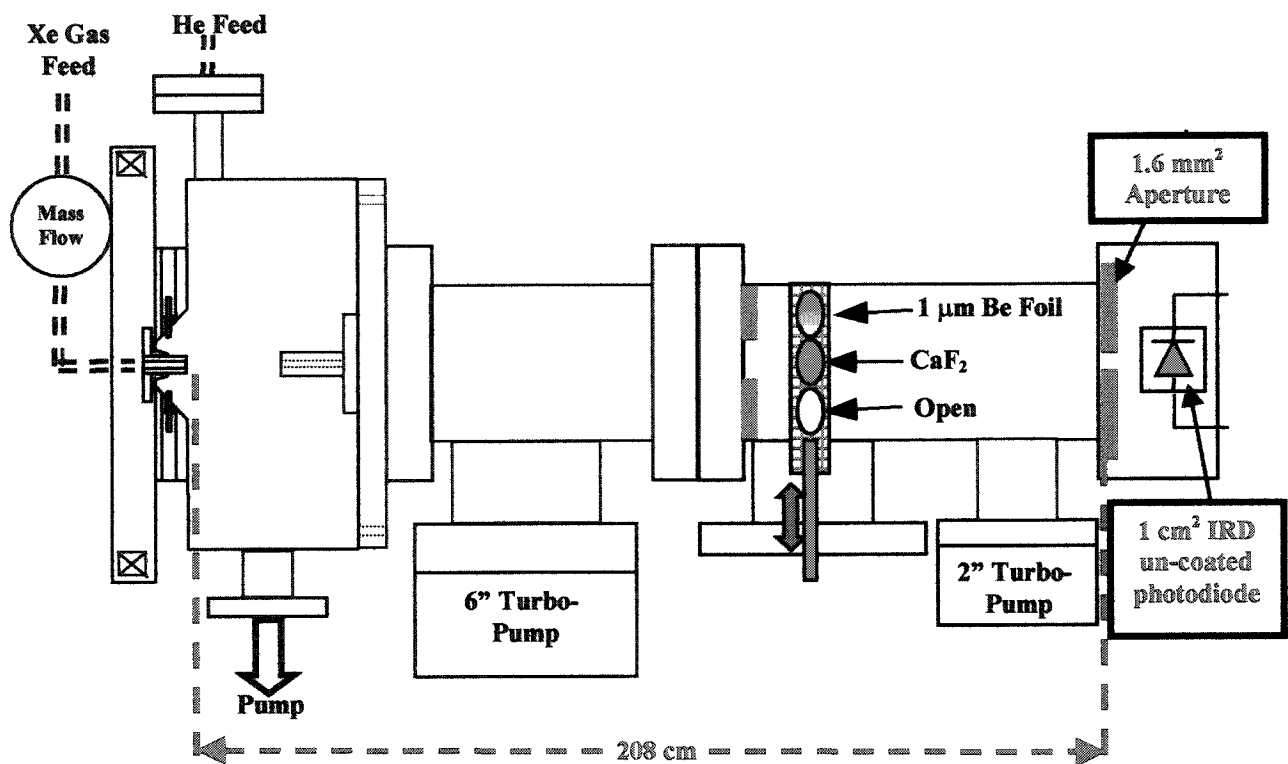


Fig 15. Experimental setup used to measure out-of-band radiation.

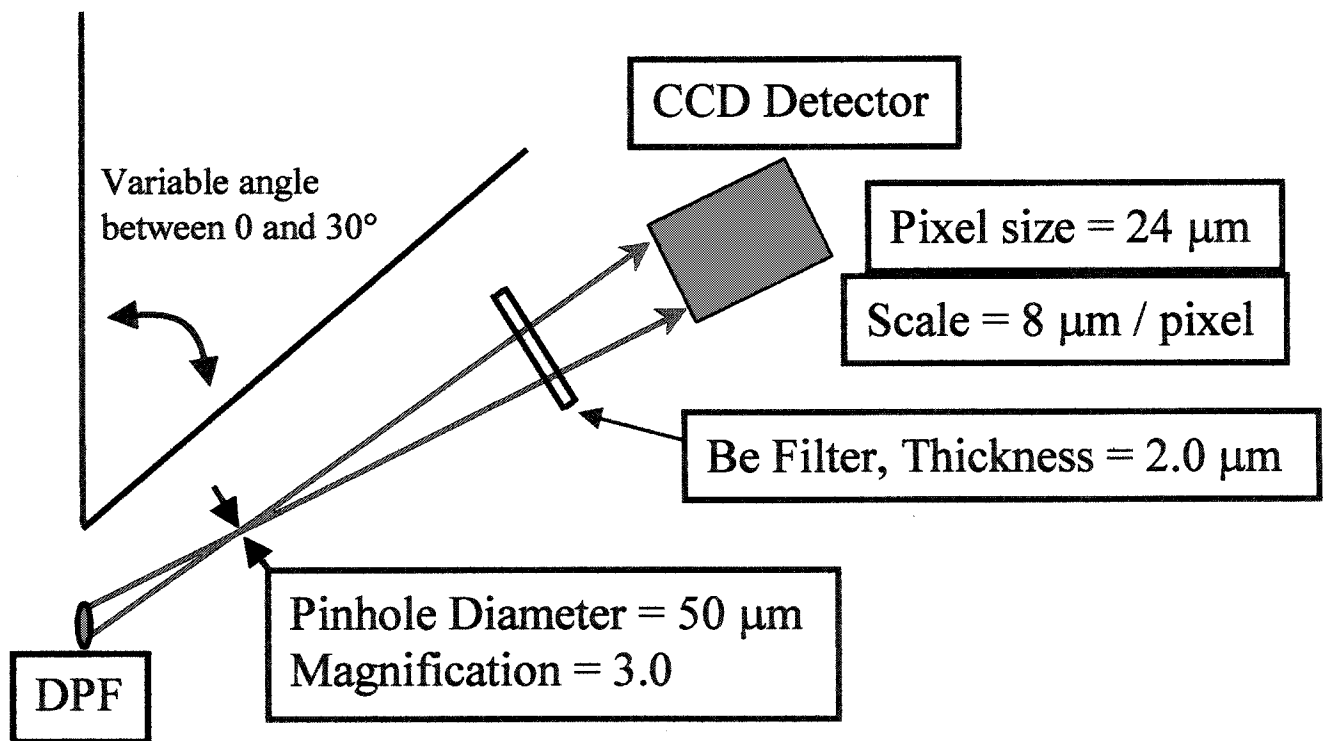


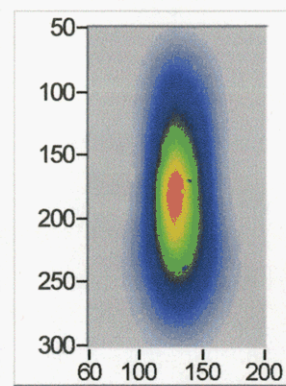
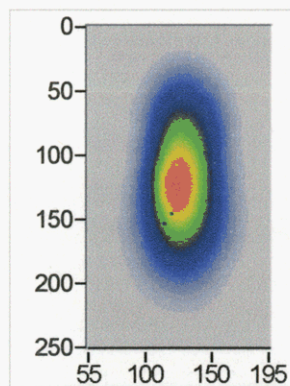
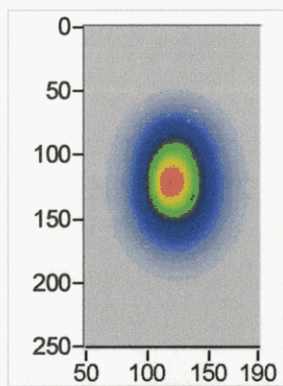
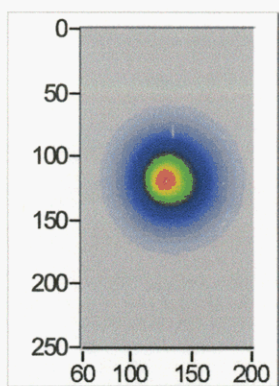
Fig 16. Pinhole camera setup for recording EUV source images.

Angle = 0 deg.

10 deg.

20 deg.

30 deg.



FWHM = 0.26 mm

0.29 mm

0.29 mm

0.25 mm

FWHM along the axis = 1.7 mm

Fig 17. Measured source images for several angles off-axis with Xenon source gas.

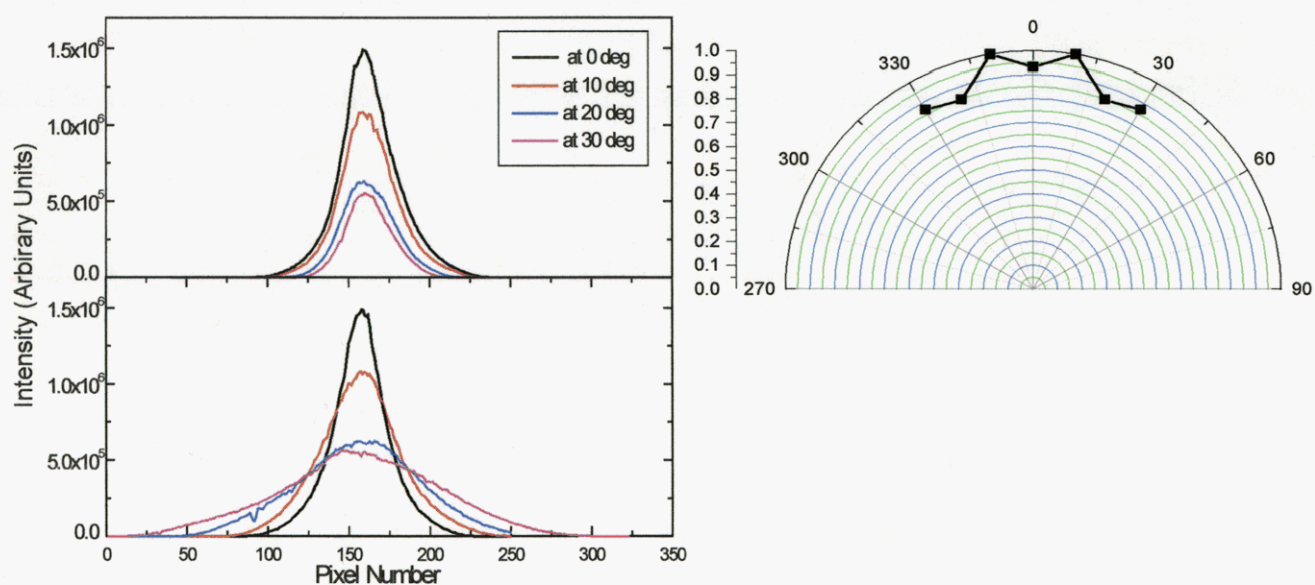


Fig 18. Measured EUV source profiles and a polar plot of the integrated emission at each angle.

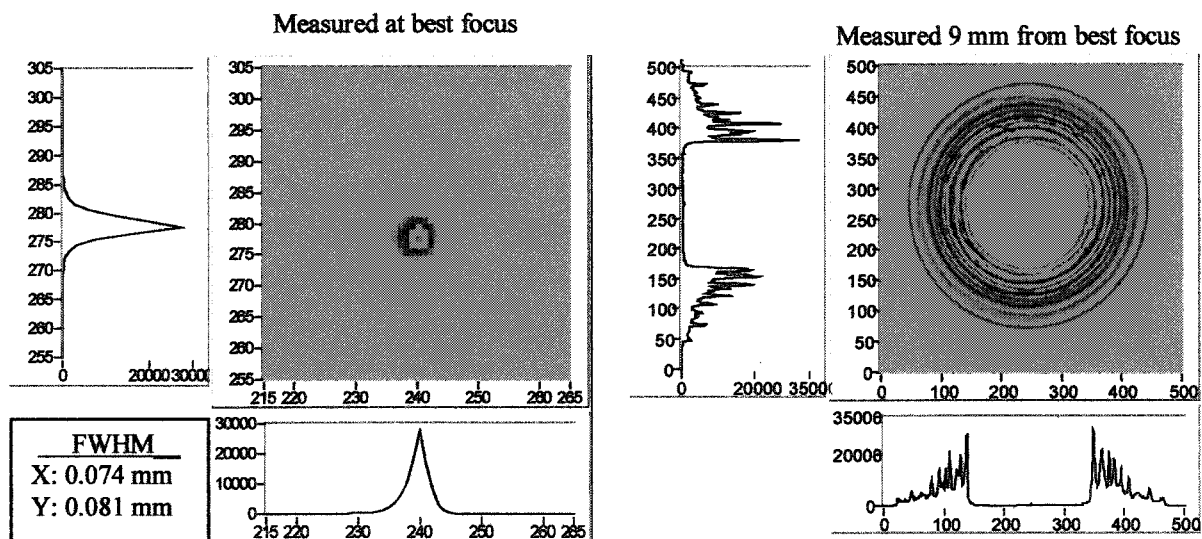
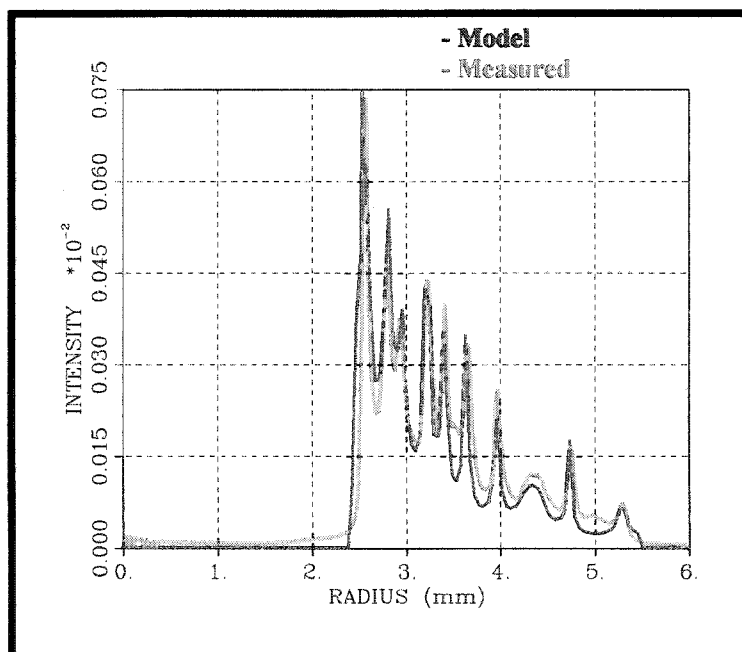


Fig19. Measured images formed with elliptical grazing incidence collector; at best focus and 9mm from best focus.



| dist front mm | Amp micron | FWHM mm |
|---------------------|---------------|------------|
| -3 | 1 | 8 |
| 2 | 1 | 9 |
| 16.5 | 0.85 | 8 |
| 21 | 0.5 | 8 |
| 26.5 | 0.9 | 8 |
| 33.5 | 1 | 8 |
| 41 | -0.5 | 8.5 |
| 49 | -1 | 7.5 |
| 57.5 | -1.15 | 7.5 |
| 67 | -1 | 6 |
| 75 | -1.6 | 10 |
| 81.5 | -2.2 | 10 |
| 87.5 | -2 | 6 |
| 96.5 | -1.3 | 5.5 |

Fig 20. Results of ray-trace modeling of the perturbed elliptical surface.